Energy materials

Fe-substituted Mn-based Prussian white as cathode for high-performance potassium-ion battery

Xuanjin Chen[1], Yang Xia[1], Xiangpeng Fang[2], Kaicheng Zhang[1], Yuli Xiong[1], and Zelang Jian[1,*]

[1] State Key Laboratory of Advanced Technology for Materials Synthesis and Processing, School of Materials Science and Engineering, Wuhan University of Technology, Wuhan 430070, China
[2] Sichuan Shenghonghui New Energy Technology Co., Ltd, Suining, China

ABSTRACT

Prussian white (PW) has a stable three-dimensional frame structure and large ion migration channels, which has been widely studied as the cathode materials for potassium-ion batteries (PIB) in recent years. The multi-composition in PWs has a great impact on the electrochemical performance as cathode materials. In this work, we investigated the relationship between Fe substitution content and electrochemical properties. The sample of PW with 10%Fe substitution shows the overall optimum electrochemical performance, which delivers a high reversible capacity of 124.3 mAh g^{-1} and capacity retention of 70.0% after 200 cycles at 100 mA g^{-1}, as well as 77.5 mAh g^{-1} at a large current density of 500 mA g^{-1}. Actually, partial Fe substitution could effectively stabilize the lattice structure and improve electrochemical properties. This work provides a practical strategy to synthesize PWs with stable crystal structure and preferable performance, which could serve as a reference for the electrochemical improvement of electrode materials.

🍎 Springer

GRAPHICAL ABSTRACT
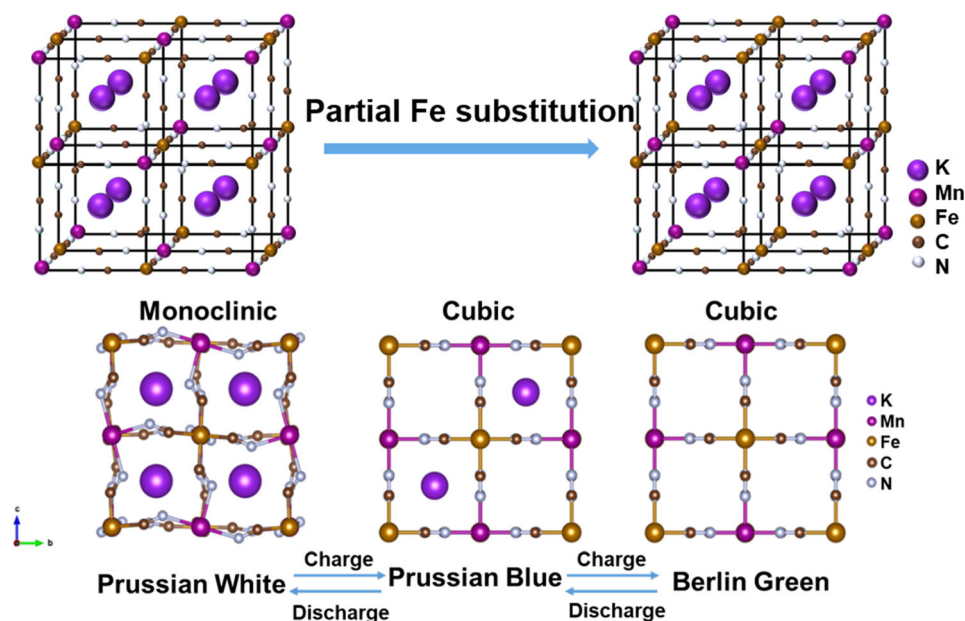
Introduction

With the development of society and technology, an increasing demand for energy especially renewable resources requires the growth of renewable energy storage devices. Among them, potassium-ion battery (PIB) is an emerging and developing technical field in recent years [1–4]. Relative to lithium, the abundant storage and low cost of potassium are great advantages [5–7]. However, the large radius of potassium leads to the slow diffusion in electrode materials and structural collapse in frequent insertion and extraction of K^+ [8]. Up to now, most cathode researches on PIBs have mainly focused on Prussian blue analogues [9, 10], polyanionic compounds [11, 12], layered oxides [13, 14] and organic compounds [15, 16]. Among them, Prussian blue analogues (PBAs) with large three-dimensional frame structure have attracted much attention as the cathode materials in recent years [17–19]. Meanwhile, the simple, low-cost and nontoxic preparation also makes PBAs the competitive potassium storage cathode materials [20].

Prussian white (PW), as a kind of Prussian blue analogue, has high K^+ content resulting in a high capacity [21]. The chemical formula of the PWs is $A_xB[M(CN)_6]_y \cdot \square_{1-y} \cdot zH_2O$, where A represents an alkalion ion (Li, Na, K), B represents a transition metal (Mn, Fe, Co, Ni, Cu) bonded with N and M represents another transition metal (usually Fe) bonded with C [22–24]. $\square$ represents the vacancies of the $M(CN)_6$ structure. H_2O contains zeolitic water and coordinated water, where the former one locates in the octahedral center of $M(CN)_6$ and the later one coordinates with M [25]. The $K_xB[Fe(CN)_6]_y \cdot \square_{1-y} \cdot zH_2O$ exhibits various properties when the transition metal B is tuned [26]. For instance, when the transition metal is Ni or Cu, these elements exhibit electrochemical inertness. Fe connected to C in $[Fe(CN)_6]$ can undergo redox reactions, accompanied by one K^+ (de)intercalation. Therefore, PWs with inert element show a relatively low capacity. Meanwhile, due to only one redox active site and low deintercalated K^+ in $K_2Ni[Fe(CN)_6]$, the crystal lattice volume changes a little during the charge/discharge process. Therefore, the crystal structure is stable, leading to good cycle performance as cathode materials. When the transition metal is Fe or Mn, PWs can exhibit two redox sites with two K^+ (de)intercalation and eventually

provide a theoretical capacity of more than 150 mAh g^{-1}. However, due to the high deintercalated K$^+$, the phase and the crystal lattice volume changes greatly during the charge/discharge process, which would damage the crystal structure of the material and affect the electrochemical performance.

Therefore, the stable structure during K$^+$ insertion/extraction greatly impacts on the electrochemical performance. Similar to the role of Fe/Co/Ni substitution in Na-based PW cathodes [27–31], transition-metal element substitution is also a remarkably effective strategy to stabilize lattice structure and improve electrochemical performance in PIBs. Some researchers used Ni to substitute the Fe bonded with N in K$_2$Fe[Fe(CN)$_6$] and found that it can balance the structural disturbances during K$^+$ insertion/extraction and greatly improve the cycle stability. Meanwhile, the introduction of Ni can activate Fe ions bonded with C and increase its capacity contribution on account that Ni^{2+} with great electronegativity has a certain inducing effect on Fe^{2+} [32]. Some researchers also introduced Ni in K$_2$Co[Fe(CN)$_6$], which also improved the cycle and rate performance [33]. Similarly, the Fe substitution could also stabilize the lattice structure and reduce the lattice distortion on account of the Jahn–Teller effect in aqueous potassium-ion batteries [34, 35]. Here, we investigated the influence of Fe substitution in Mn-based PW (K$_2$Mn[Fe(CN)$_6$]) in nonaqueous potassium-ion batteries. We synthesized K$_x$Fe$_a$Mn$_{1-a}$[Fe(CN)$_6$]$_y$-zH$_2$O samples (a = 0, 0.05, 0.1, 0.15, 0.3 and 0.5, named as KMF, 5%Fe-KMF, 10%Fe-KMF, 15%Fe-KMF, 30%Fe-KMF, 50%Fe-KMF, separately). The influence of different Fe substitution content on the performance of potassium storage was researched and the appropriate Fe substitution KMF shows good cycling and high rate performance.

Material and methods

Material preparation

All Fe-KMF samples were synthesized by a gentle coprecipitation method. 25 mmol C$_6$H$_5$K$_3$O$_7$·H$_2$O (99.5%, Sinopharm Chemical Reagent Co., Ltd.) and 5 mmol MnCl$_2$·4H$_2$O (99%, Sinopharm Chemical ReagentCo., Ltd.) mixed with different proportions of FeCl$_2$·4H$_2$O (99%, Sinopharm Chemical ReagentCo., Ltd.) were dissolved in 50 mL deionized water. The

solution was stirred for 30 min under nitrogen atmosphere named solution A. Similarly, 125 mmol KCl (99.8%, Sinopharm Chemical Reagent Co., Ltd.) and 5 mmol K$_4$Fe(CN)$_6$·3H$_2$O (99%, Sinopharm Chemical Reagent Co., Ltd.) were dissolved in 50 mL deionized water and stirred for 30 min at 40 °C in N$_2$ atmosphere to form solution B. Then, the solution A was dropwise added (1 mL/min) to B and strongly stirred at 40 °C with nitrogen constantly flowing. After 2 h, the mixed solution was further aged at 40 °C for 2 h to acquire uniform grains. The whole synthesis process was under nitrogen atmosphere to avoid oxidation. After that, the formed precipitate was centrifuged and washed with deionized water for three times. Finally, the product was obtained by vacuum drying at 80 °C overnight.

Structural characterization

The powder X-ray diffraction (XRD) patterns were collected by PANalytical diffractometer using Cu-Kα radiation at a scan rate of 5°/min at a 2θ range of 10–80°. The electrode wafers for ex situ XRD were disassembled from the batteries, washed by the electrolyte and vacuum-dried overnight. The batteries were charged/discharged at 100 mA g^{-1} and reached the set charge/discharge state previously. The morphologies of the Fe-KMFs were observed by scanning electron microscope (SEM) on Zeiss Ultra Plus scanning microscopy. Transmission electron microscope (TEM) images were recorded on JEOL 2100F. Fourier transform infrared (FTIR) spectroscopy was performed on Nicolet6700 spectrometer between 4000 and 400 cm^{-1}. Inductively coupled plasma-optical emission spectrum (ICP-OES) was carried out on Prodigy 7. Thermogravimetric analysis (TGA) was conducted on STA449F3 instrument heating from 40 to 800 °C at 5 °C/min under nitrogen atmosphere.

Electrochemical characterization

Fe-KMF, super P and CMC-Na were mixed at a weight ratio of 7:2:1 to a total of 100 mg and then stirred for 6 h to form a uniform slurry. CMC-Na was used as binder due to its suitability. Using aluminum foil as a collector, the slurry was pasted on its surface evenly, dried at 80 °C under vacuum overnight and then cropped into wafers (diameter 12 mm) with a mass loading of about 1.0 mg/cm^2. 0.8 M potassium

hexafluorophosphate (KPF_6) in propylene carbonate (PC) with 10% fluoroethylene carbonate (FEC) was used as electrolyte in this study. Glass fiber (Whatman, Grade GF/B) was used as separators. The half-cell using CR2032 was assembled in a nitrogen glovebox with oxygen and moisture below 0.1 ppm.

Results and discussions

Structural and morphological characterization

Prussian whites with Fe substitution were prepared by a coprecipitation method. As shown in Fig. S1, PWs have large frame structure, where K^+ ions locate in the interstitial position of $Mn–N\equiv C–Fe$ octahedron. The XRD patterns (Fig. 1a) of all samples belong to KMF, which are monoclinic system with space group $P2_1/c$. Meanwhile, no impurity peaks appear in their XRD patterns, but some changes emerge. Figure 1b shows the partial enlarged XRD patterns of Fe-KMFs. All three strong peaks at $2\theta = 17.5$, 24.9 and 35.5° shift to high angles to a certain extent, indicating their interplanar spacing d decreases. In spite of the same coordination number

(CN = 6), the effective ion radius of Fe^{2+} (0.78 Å) is smaller than that of Mn^{2+} (0.83 Å). Therefore, when Fe^{2+} partially replaces the Mn^{2+}, the crystal lattice would decrease. FTIR spectrums of Fe-KMFs are shown in Fig. 1c. The presence of Fe-KMFs is verified by the absorption peaks at 595, 1640, 2066 and 3430 cm^{-1}. The absorption peaks at 3430 and 1640 cm^{-1} represent the stretching vibration and bending vibration of the O–H, indicating the existence of H_2O in Fe-KMFs or environmental water. The absorption peak at 2066 cm^{-1} reveals the cyanide stretching vibration of $C\equiv N$. The absorption peak at 595 cm^{-1} in the fingerprint region reflects the stretching vibration of the Fe–C skeleton, verifying the coordination of Fe atoms and C atoms. The above spectrums indeed confirm the $Fe/Mn–N\equiv C–Fe$ octahedral structure in Fe-KMFs.

In order to obtain the exact chemical formula of Fe-KMFs and the content of $[Fe(CN)_6]$ vacancy and H_2O, ICP-OES and TGA were conducted. The contents of K, Mn, Fe and H_2O were tested, and results are shown in Table 1 (TG curves are shown in Fig. S2). The chemical formula of the samples can be written as $K_xFe_aMn_{1-a}[Fe(CN)_6]_y \cdot \square_{1-y} \cdot zH_2O$, where a is 0, 0.05, 0.1, 0.15, 0.3, 0.5. According to the formula (1) and (2), the actual chemical formulas are

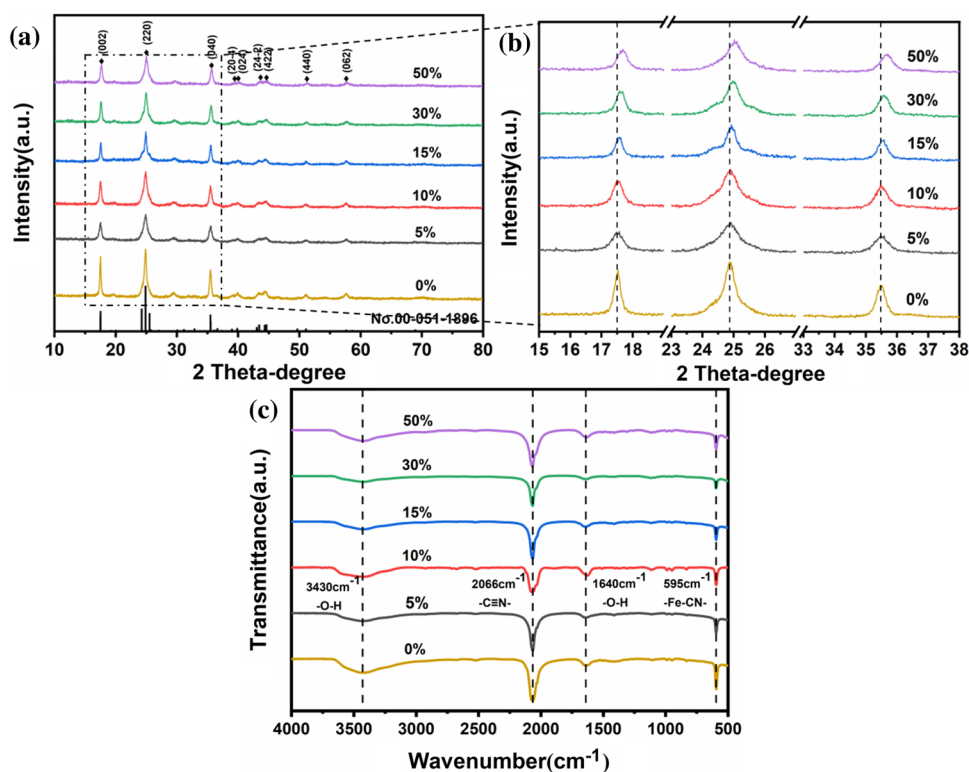**Figure 1** **a** XRD patterns and **b** partial enlarged XRD patterns of Fe-KMFs. **c** FTIR spectrums of Fe-KMFs.

Table 1 ICP-OES and TGA results of Fe-KMFs

	K (wt%)	Mn (wt%)	Fe (wt%)	H_2O (wt%)
KMF	18.02	12.75	12.71	1.83
5%Fe-KMF	16.71	12.83	13.12	1.67
10%Fe-KMF	17.34	11.79	14.24	1.47
15%Fe-KMF	16.85	11.68	14.59	1.65
30%Fe-KMF	16.22	9.79	16.73	2.27
50%Fe-KMF	16.12	6.86	18.74	2.37

$K_{1.99}Mn[Fe(CN)_6]_{0.98}\cdot\square_{0.02}\cdot0.44H_2O$, $K_{1.74}Mn_{0.95}Fe_{0.05}[Fe(CN)_6]_{0.91}\cdot\square_{0.09}\cdot0.38H_2O$, $K_{1.87}Mn_{0.90}Fe_{0.1}[Fe(CN)_6]_{0.97}\cdot\square_{0.03}\cdot0.34H_2O$, $K_{1.73}Mn_{0.85}Fe_{0.15}[Fe(CN)_6]_{0.89}\cdot\square_{0.11}\cdot0.37H_2O$, $K_{1.64}Mn_{0.7}Fe_{0.3}[Fe(CN)_6]_{0.87}\cdot\square_{0.13}\cdot0.50H_2O$, $K_{1.66}Mn_{0.5}Fe_{0.5}[Fe(CN)_6]_{0.84}\cdot\square_{0.16}\cdot0.53H_2O$, respectively.

$$x = \frac{(1-a)n_K}{n_{Mn}} \tag{1}$$

$$y = \frac{(1-a)n_{Fe}}{n_{Mn}} - a \tag{2}$$

The contents of H_2O and $[Fe(CN)_6]$ vacancies slightly increase when Fe content is more than 10%. It is inferred that the Fe ions constantly introduced competes with Mn ions for $[Fe(CN)_6]$. The defects increase due to the synergistic effect of the Fe and Mn ions. Meanwhile, water molecules are likely to enter the crystal structure, resulting in the H_2O content increasing.

Figure 2 shows the SEM images of Fe-KMFs. KMF has cubic morphologies and clear boundaries with edge length of 50 ~ 70 nm, whereas other Fe-KMFs are all irregular spheres or cuboids. Partial Fe substitution reduces the particle size. With more Fe content, the average grain size of Fe-KMFs decreases gradually from 60 nm to about 20 nm. Meanwhile, small particles' agglomeration is further obvious, which is conducive to the infiltration of the electrolyte and the transmission of ions. TEM was performed as shown in Fig. 3a. 10%Fe-KMF possesses a cube morphology with an average size of 40 nm. Figure 3b is a selected area electron diffraction (SAED) image of 10%Fe-KMF. It is composed of a series of bright and clear concentric rings, indicating that it has good crystallinity and the diffraction pattern shows polycrystalline characteristics, which can be indexed to the to the (002), (220) and (040) crystal planes, respectively.

Electrochemical characterization

Galvanostatic charge/discharge test was performed on Fe-KMFs, which were tested at a voltage range of 2.5 ~ 4.5 V vs. K/K^+ and current density of 100 mA g^{-1}. As shown in Fig. 4a, 10% Fe-KMF

Figure 2 SEM images of Fe-KMFs: **a** KMF, **b** 5%Fe-KMF, **c** 10%Fe-KMF, **d** 15%Fe-KMF, **e** 30%Fe-KMF and **f** 50%Fe-KMF.
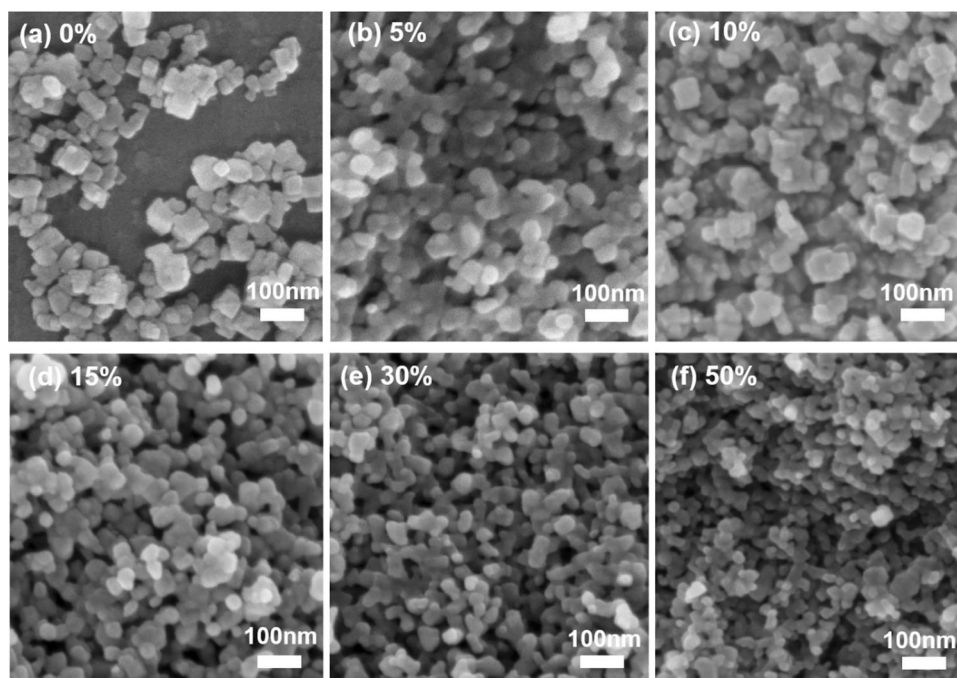
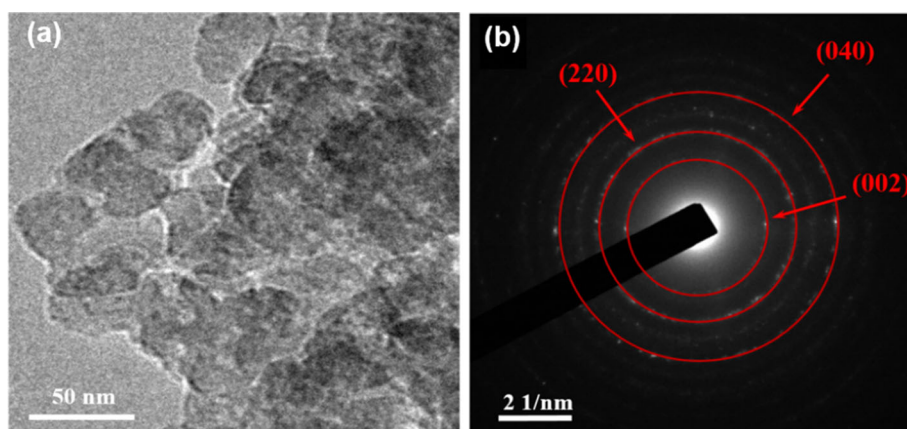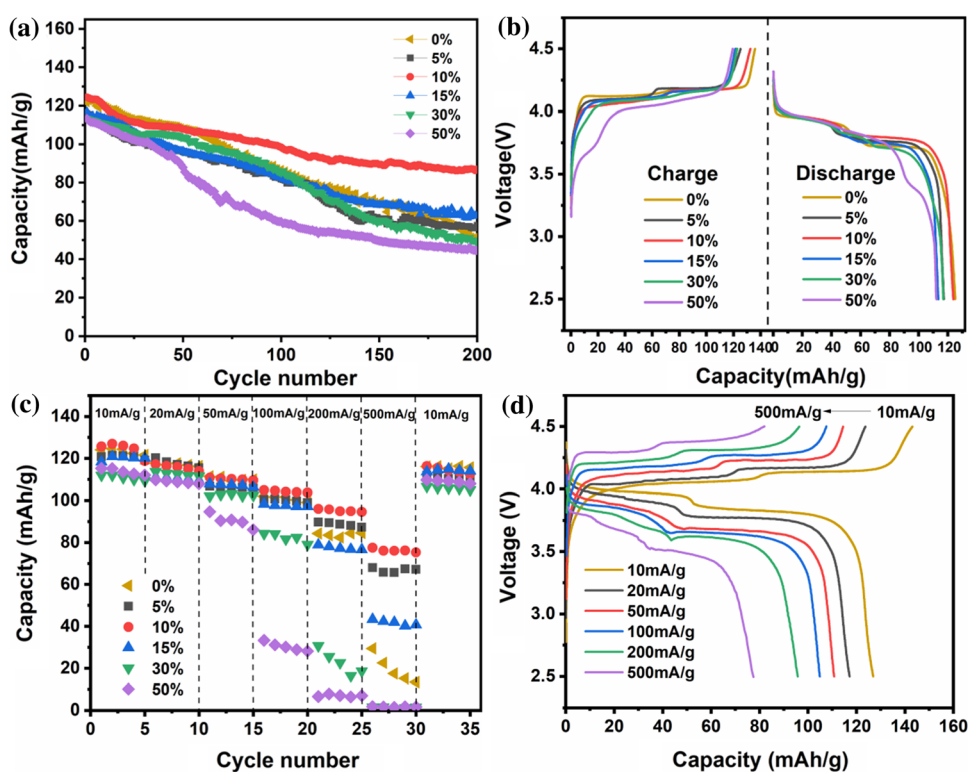**Figure 3 a** TEM image and **b** SAED image of 10%Fe-KMF.

Figure 4 a Cycle performance of Fe-KMFs at a current destiny of 100 mA g^{-1}. **b** Charge - discharge curves of Fe-KMFs' electrodes between 2.5 and 4.5 V at 100 mA g^{-1}. **c** Rate performance of Fe-KMFs. **d** Charge–discharge curve of 10%Fe-KMF electrode from 10 to 500 mA g.$^{-1}$.

shows the optimum overall performance in terms of both capacity and cycling stability. It exhibits the highest initial reversible capacity of 124.3 mAh g^{-1} and capacity retention of 70.0% after 200 cycles. The cycling stability of 10%Fe-KMF is much higher than that of pure Mn-based KMF (42.6%). In pure Mn-based KMF, some Mn ions and Fe ions would dissolve in the electrolyte during long cycle, leading that the crystal structure gradually collapses and the capacity is quickly lost. Moreover, Mn^{3+} could lead to the distortion of the crystal lattice due to the Jahn–Teller effect and affect K$^+$ (de)intercalation during

the redox process. Instead, the partial Fe ions substitution could relieve the Jahn–Teller effect of Mn^{3+} and stabilize the lattice structure [34]. Therefore, its cycling stability remarkably improves. The remaining electrodes of 5%Fe-KMF, 15%Fe-KMF, 30%Fe-KMF and 50%Fe-KMF have similar initial discharge capacities of 115.8, 116.9, 113.4 and 113.3 mAh g^{-1}. Their capacity retentions are 49.8, 53.5, 42.9 and 39.4%, respectively. More Fe ions substitution should improve the stability of the lattice structure more obviously. However, due to the synergistic effect of the Fe and Mn ions, the vacancy defects and crystal

water also increase. Instead, it damages the integrity of the crystal structure and deteriorates the electrochemical performance. From our experiment results, 10% is the appropriate Fe substitution content.

Figure 4b shows the charge and discharge curves of Fe-KMFs at 100 mA g^{-1}. Two charge plateaus appear at around 4.1 and 4.2 V for 5%Fe-KMF, 10%Fe-KMF and 15%Fe-KMF in the charge process, which are similar to that of KMF, corresponding to the oxidation of Fe^{2+} to Fe^{3+} and Mn^{2+} to Mn^{3+} with two K^+ extraction. However, with Fe content increasing, there is only one charge plateau above 4.1 V for 30%Fe-KMF. Moreover, a small charge plateau at around 3.75 V appears for 50%Fe-KMF. It is indicated that with partial Mn ions replaced by Fe ions, the capacity contributed by the oxidation reaction at around 4.2 V is reduced and merged; instead, alternative Fe ions undergo a redox reaction at around 3.75 V. Furthermore, in the discharge profile of 50%Fe-KMF, a small plateau appears at around 3.25 V, which also confirms this phenomenon.

The rate performance of Fe-KMFs is shown in Fig. 4c. The voltage range was 2.5 ∼ 4.5 V vs. K/K$^+$, and the current density increased from 10 to 500 mA g^{-1} and returns to 10 mA g^{-1} eventually. 10%Fe-KMF still displays the outstanding rate capability. It delivers a discharge capacity of 126.9 mAh g^{-1} at 10 mA g^{-1} and retains 77.5 mAh g^{-1} at a high current density of 500 mA g^{-1}. Meanwhile, the capacity recovers to 116.3 mAh g^{-1} when the current density returns back to 10 mA g^{-1}, demonstrating minimal damage to the crystal structure of 10%Fe-KMF. It is inferred that 10%Fe-KMF has a small grain size due to Fe substitution, which is beneficial to the K^+ diffusion within the short distance. Therefore, in contrast to pure Mn-based KMF, Fe-KMFs have a large ion diffusion rate, which contributes to its rate performance. However, 30%Fe-KMF and 50%Fe-KMF electrodes have almost no capacities at 500 mA g^{-1}. This could be due to too much internal defects in the material, which leads to few redox reactions at high current density. Figure 4d shows the charge and discharge curves of 10%Fe-KMF at various current densities. As the current density increases, the electrode polarization increases and the discharge plateau decreases clearly. Yet at high current density, the discharge voltage also maintains at about 3.5 V, which could effectively maintain the battery's output voltage.

In order to further investigate the electrochemical reaction process, CV was performed on Fe-KMFs (other CV curves are shown in Fig. S3). The voltage range was 3.0 ∼ 4.5 V, and the scanning rate was 0.1 mV s^{-1}. As shown in Fig. 5a, CV curve of 10%Fe-KMF presents a single merged oxidation peak and two reduction peaks, indicating two pairs of redox sites. In the charge process, a single oxidation peak appears at around 4.28 V because the potentials of the two peaks are very close, merging to a large peak. In the discharge process, the reduction peak at around 3.85 V can be ascribed to the high-spin Mn^{3+}/Mn^{2+} coordinated with N, and another reduction peak at about 3.65 V can be assigned to low-spin Fe^{3+}/Fe^{2+} coordinated with C. However, no redox peak is observed for the Fe^{3+}/Fe^{2+} bonded with N, which is also consistent with the charge and discharge curve of 10%Fe-KMF. This could be due to low Fe substitution content. EIS was carried out between 100 mHz and 100 kHz at an AC voltage amplitude of 5 mV. Figure 5b shows the EIS of Fe-KMFs, and the equivalent circuit is shown in the small figure embedded in Fig. 5b. The EIS curves of Fe-KMFs are similar to that of KMF. The EIS curves of Fe-KMFs are also composed of a semicircle in the high-frequency region and a slash in the low-frequency region. The fitted results are shown in Table 2. 10%Fe-KMF possesses the smallest charge transfer resistance (R_{ct}), which is beneficial to the transmission of electrons. This result also accounts for the optimal rate performance of 10%Fe-KMF.

To explore the potassium storage mechanism and verify the structural stability of 10%Fe-KMF during charge and discharge process, ex situ XRD was performed. Figure 6a shows the XRD patterns in selected states, corresponding to charge/discharge curves in Fig. 6b. During the charge process (i.e., state 1 ∼ 4), the three strong peaks of 10%Fe-KMF at 17.5, 24.9 and 35.5° all shift to low angle. Take the peak at 35.5° for example, the peak intensity gradually weakens and a new peak appears at 34.2° in the charge process. When it reaches the state 4 (fully charged state), the peak at 35.5° disappears completely and the peak intensity at 34.2° reaches the maximum. At this time, 10%Fe-KMF has changed from the monoclinic phase to the cubic phase completely. During the discharge process, just opposite to that of charge process, the cubic phase transforms into a mixture of the cubic phase and the monoclinic phase, then completely back to the monoclinic phase. After a cycle, the XRD

Figure 5 a Cyclic voltammetry (CV) curve of 10%Fe-KMF at 0.1mV s^{-1}. **b** Electrochemical impedance spectra (EIS) of Fe-KMFs.
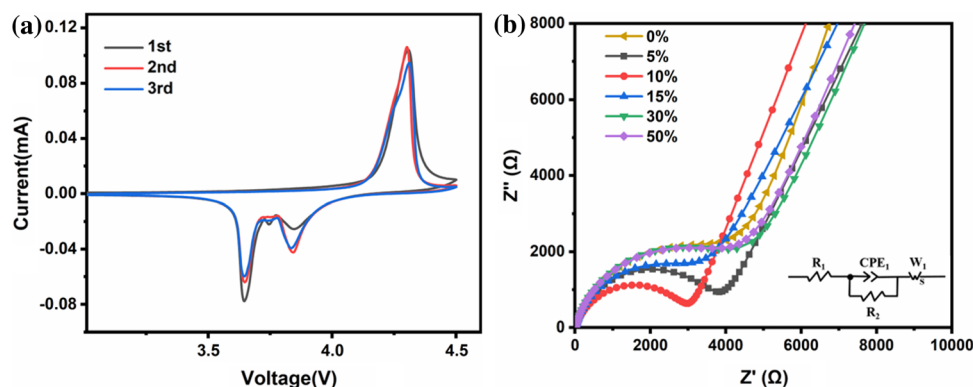

Table 2 EIS results of Fe-KMFs

	R_s (Ω)	R_{ct} (Ω)
KMF	6.5	4297
5%Fe-KMF	6.7	3765
10%Fe-KMF	6.5	3003
15%Fe-KMF	7.1	3191
30%Fe-KMF	6.4	4273
50%Fe-KMF	6.5	4289

patterns goes back to the initial state, indicating that 10%Fe-KMF has a stable crystal lattice during the insertion and extraction of K$^+$ ions and the phase transition is highly reversible. Figure 6c reveals the phase transition mechanism of 10%Fe-KMF during the charge and discharge process. The sample changes from monoclinic Prussian white to cubic Prussian blue with the extraction of one K$^+$ and eventually to cubic Berlin green with the extraction of another K$^+$; the discharge process is contrary to the charge process, and the material changes from cubic Berlin green, cubic Prussian blue and then to monoclinic Prussian white by inserting two K$^+$. Komaba reported that pure Mn-based Prussian white would change from monoclinic phase to cubic phase during the charge process, but due to the Jahn–Teller effect of Mn^{3+}, the phase would eventually become tetragonal [36]. The cooperative Jahn–Teller distortion of Mn^{3+} makes the reduction reaction of Mn^{3+} difficult and impacts the stability of the lattice structure [37]. Here, partial Fe^{2+} substitution not only decreases the density of Mn^{3+} in the lattice, but 10%Fe-KMF only undergoes the two-phase transformation between the monoclinic phase and cubic phase, illustrating that the Fe substitution can stabilize the lattice structure, reduce the cooperative Jahn–Teller distortion and

activate the Mn^{2+}/Mn^{3+}-N redox reaction. Based on the above two roles, 10%Fe-KMF exhibits a remarkable improvement in cycle stability.

To explore the electrochemical kinetics and verify the large ion diffusion rate of 10%Fe-KMF in the redox reaction, CV tests were carried out at different scanning rates (0.1, 0.2, 0.3, 0.4, 0.5, 0.8 and 1 mV s^{-1}) and the results are shown in Fig. 7a. The redox peaks in the CV curve are unchanged, and the redox sites are still Fe and Mn ions. The oxidation peak shifts to high voltage, and the reduction peak moves to low voltage as the scan rate increases. The peak currents keep increasing at the same time. The diffusion coefficient of K$^+$ at the peak current is calculated according to the Randles–Sevcik formula (3):

$$I_p = 268600 \times n^{\frac{3}{2}} A D^{\frac{1}{2}} v^{\frac{1}{2}} C \qquad (3)$$

where I_P is the peak current (A), n is the number of transferred electrons, A is the reaction area of electrode (cm^2), C is the concentration of alkali metal ions in the electrolyte (mol cm^{-3}), v is the voltage scanning rate (V s^{-1}) and D is the diffusion coefficient of alkali metal ions (cm^2 s^{-1}). In our experiment, the number of transferred electrons is 2, the reaction area of electrode is 0.5, and the concentration of KPF$_6$ electrolyte is 0.8. A straight line is obtained by plotting square root of the scan rate $\left(v^{\frac{1}{2}}\right)$ and peak current (I_P) as the abscissa and ordinate. According to the formula (3), the diffusion coefficient of K$^+$ at the oxidation reaction is 8.35×10^{-10} cm^2 s^{-1}. Similarly, the diffusion coefficient of K$^+$ in the reduction reaction is 2.33×10^{-9} cm^2 s^{-1}. It is certain that the Fe-KMF has a large ion diffusion rate, which could be related to small grain size. When the grain size is small, K$^+$ diffuses easily between the electrode particles, exhibiting a high diffusion coefficient.

Figure 6 **a** Ex-situ XRD, **b** charge–discharge curve and **c** structure transition illustration of 10%Fe-KMF.
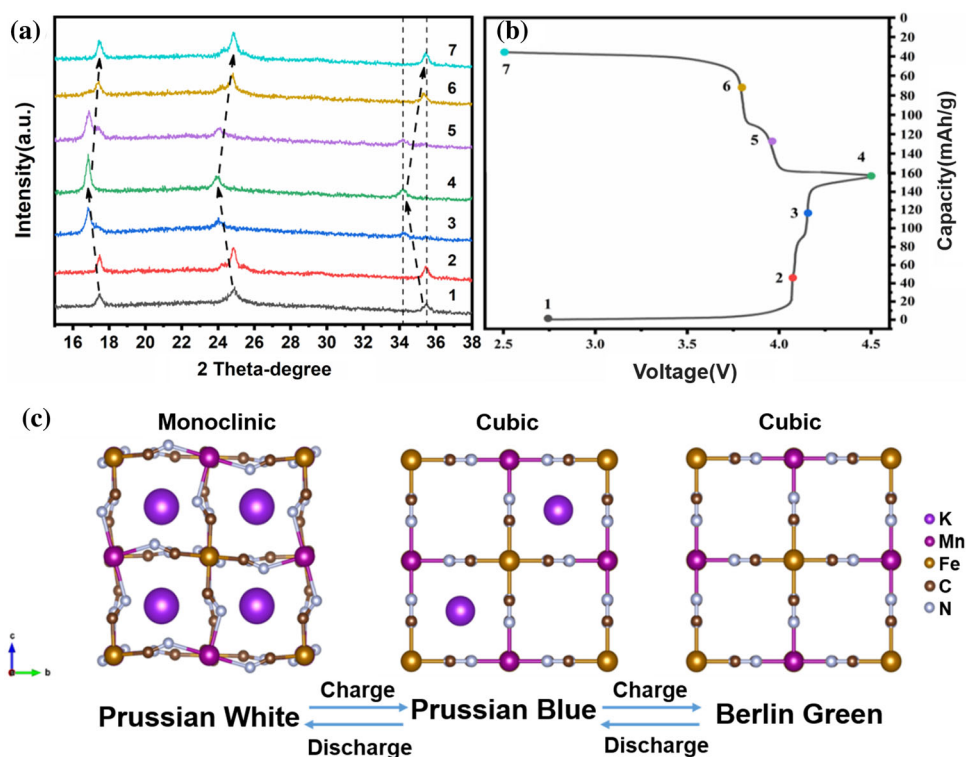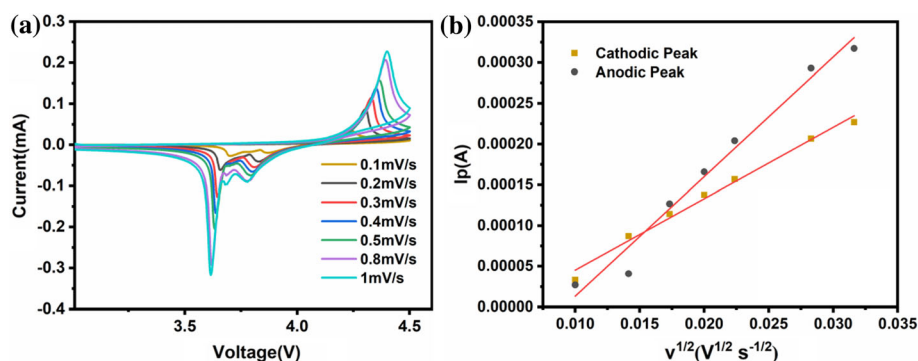

Figure 7 **a** Cyclic voltammetry curves of 10%Fe-KMF at different scanning rates. **b** Fitting curve of the peak current (I_p) and the square root of the scanning voltage $\left(v^{\frac{1}{2}}\right)$ of 10%Fe-KMF.

Conclusions

In summary, $K_xFe_aMn_{1-a}[Fe(CN)_6]_y \cdot zH_2O$ was prepared by a simple coprecipitation process. Among them, 10%Fe-KMF delivers the highest initial reversible capacity of 124.3 mAh g^{-1} and capacity retention of 70.0% after 200 cycles at 100 mA g^{-1}. Meanwhile, 10%Fe-KMF shows the best rate performance, which still delivers the capacity of 77.5 mAh g^{-1} at a high current density of 500 mA g^{-1}. Via the ex situ XRD and CV tests at different scanning rates on 10%Fe-KMF, it is certain that the Fe substitution stabilizes the lattice structure and reduces the Jahn–Teller effect of Mn, and thus 10%Fe-KMF only

changes between the monoclinic phase and the cubic phase in the charge/discharge process. Meanwhile, 10%Fe-KMF with small grain size also has high K$^+$ diffusion coefficient. However, with the Fe content increasing, vacancy defects and crystal water also increase, which damage the integrity of the crystal structure and deteriorate the electrochemical performance. Therefore, 10%Fe-KMF exhibits the overall optimum electrochemical performance. This work provides a simple coprecipitation method to synthesize Fe-KMFs with stable crystal structure and excellent performance, which also accounts for the promising strategy of transition-metal substitution.

Acknowledgements

Author contributions

The manuscript was written through contributions of all authors. All authors have given approval to the final version of the manuscript.

Declarations

Conflict of interest The authors declare that they have no competing financial interest.

Supplementary Information: The online version contains supplementary material available at https://doi.org/10.1007/s10853-022-07430-2.

References

[1] Eftekhari A (2004) Potassium secondary cell based on Prussian blue cathode. J Power Sources 126:221–228. https://doi.org/10.1016/j.jpowsour.2003.08.007

[2] Jian Z, Luo W, Ji X (2015) Carbon electrodes for K-ion batteries. J Am Chem Soc 137:11566–11569. https://doi.org/10.1021/jacs.5b06809

[3] Jian Z, Xing Z, Bommier C, Li Z, Ji X (2016) Hard carbon microspheres: potassium-ion anode versus sodium-ion anode. Adv Energy 6:1501874–15018748. https://doi.org/10.1002/aenm.201501874

[4] Wu X, Leonard DP, Ji X (2017) Emerging non-aqueous potassium-ion batteries: challenges and opportunities. Chem Mater 29:5031–5042. https://doi.org/10.1021/acs.chemmater.7b01764

[5] Rajagopalan R, Tang Y, Ji X, Jia C, Wang H (2020) Advancements and challenges in potassium ion batteries: a comprehensive review. Adv Funct Mater 30:1909486–1909520. https://doi.org/10.1002/adfm.201909486

[6] Min X, Xiao J, Fang M et al (2021) Potassium-ion batteries: outlook on present and future technologies. Energy Environ Sci 14:2186–2243. https://doi.org/10.1039/d0ee02917c

[7] Zhou A, Cheng W, Wang W et al (2021) Hexacyanoferrate-type Prussian blue analogs: principles and advances toward high-performance sodium and potassium ion batteries. Adv

Energy Mater 11:2000943–2000977. https://doi.org/10.1002/aenm.202000943

[8] Xu Z, Lv X, Chen J, Jiang L, Lai Y, Li J (2016) Dispersion-corrected DFT investigation on defect chemistry and potassium migration in potassium-graphite intercalation compounds for potassium ion batteries anode materials. Carbon 107:885–894. https://doi.org/10.1016/j.carbon.2016.06.101

[9] Chong S, Chen Y, Zheng Y et al (2017) Potassium ferrous ferricyanide nanoparticles as a high capacity and ultralong life cathode material for nonaqueous potassium-ion batteries. J Mater Chem A 5:22465–22471. https://doi.org/10.1039/c7ta08139a

[10] Jiang X, Zhang T, Yang L, Li G, Lee JY (2017) A Fe/Mn-based Prussian blue analogue as a K-rich cathode material for potassium-ion batteries. ChemElectroChem 4:2237–2242. https://doi.org/10.1002/celc.201700410

[11] Mathew V, Kim S, Kang J et al (2014) Amorphous iron phosphate: potential host for various charge carrier ions. NPG Asia Mater 6:138–147. https://doi.org/10.1038/am.2014.98

[12] Han J, Li GN, Liu F et al (2017) Investigation of $K_3V_2(PO_4)_3$/C nanocomposites as high-potential cathode materials for potassium-ion batteries. Chem Comm 53:1805–1808. https://doi.org/10.1039/C6CC10065A

[13] Vaalma C, Giffin GA, Buchholz D, Passerini S (2016) Non-aqueous K-ion battery based on layered $K_{0.3}MnO_2$ and hard carbon/carbon black. J Electrochem Soc 163:1295–1299. https://doi.org/10.1149/2.0921607jes

[14] Deng T, Fan X, Luo C et al (2018) Self-templated formation of P_2-type $K_{0.6}CoO_2$ microspheres for high reversible potassium-ion batteries. Nano Lett 18:1522–1529. https://doi.org/10.1021/acs.nanolett.7b05324

[15] Chen Y, Luo W, Carter M et al (2015) Organic electrode for non-aqueous potassium-ion batteries. Nano Energy 18:205–211. https://doi.org/10.1016/j.nanoen.2015.10.015

[16] Jian Z, Liang Y, Rodríguez-Pérez IA, Yao Y, Ji X (2016) Poly(anthraquinonyl sulfide) cathode for potassium-ion batteries. Electrochem Commun 71:5–8. https://doi.org/10.1016/j.elecom.2016.07.011

[17] He G, Nazar LF (2017) Crystallite size control of Prussian white analogues for nonaqueous potassium-ion batteries. ACS Energy Lett 2:1122–1127. https://doi.org/10.1021/acsenergylett.7b0017

[18] Husmann S, Zarbin AJG, Dryfe RAW (2020) High-performance aqueous re-chargeable potassium batteries prepared via interfacial synthesis of a Prussian blue-carbon nanotube composite. Electrochim Acta 349:136243–136270. https://doi.org/10.1016/j.electacta.2020.136243

[19] Wang Z, Zhuo W, Li J et al (2022) Regulation of ferric iron vacancy for Prussian blue analogue cathode to realize high-

performance potassium ion storage. Nano Energy 98:107243–107249. https://doi.org/10.1016/j.nanoen.2022.107243

[20] Xue L, Li Y, Gao H et al (2017) Low-cost high-energy potassium cathode. J Am Chem Soc 139:2164–2167. https://doi.org/10.1021/jacs.6b12598

[21] Wu X, Qiu S, Liu Y et al (2021) The quest for stable potassium-ion battery chemistry. Adv Mater 34:2106876–2106885. https://doi.org/10.1002/adma.202106876

[22] Luo Y, Shen B, Guo B et al (2018) Potassium titanium hexacyanoferrate as a cathode material for potassium-ion batteries. J Phys Chem Solids 122:31–35. https://doi.org/10.1016/j.jpcs.2018.06.014

[23] Chong S, Yang J, Sun L, Guo S, Liu Y, Liu HK (2020) Potassium nickel iron hexacyanoferrate as ultra-long-life cathode material for potassium-ion batteries with high energy density. ACS Nano 14:9807–9818. https://doi.org/10.1021/acsnano.0c02047

[24] Deng L, Qu J, Niu X et al (2021) Defect-free potassium manganese hexacyanoferrate cathode material for high-performance potassium-ion batteries. Nat Commun 12:2167–2175. https://doi.org/10.1038/s41467-021-22499-0

[25] Zhang C, Xu Y, Zhou M et al (2017) Potassium Prussian blue nanoparticles: a low-cost cathode material for potassium-ion batteries. Adv Funct Mater 27:1604307–1604314. https://doi.org/10.1002/adfm.201604307

[26] Wu X, Jian Z, Li Z, Ji X (2017) Prussian white analogues as promising cathode for non-aqueous potassium-ion batteries. Electrochem Commun 77:54–57. https://doi.org/10.1016/j.elecom.2017.02.012

[27] Xie B, Zuo P, Wang L et al (2019) Achieving long-life Prussian blue analogue cathode for Na-ion batteries via triple-cation lattice substitution and coordinated water capture. Nano Energy 61:201–210. https://doi.org/10.1016/j.nanoen.2019.04.059

[28] Wei C, Fu XY, Zhang LL et al (2021) Structural regulated nickel hexacyanoferrate with superior sodium storage performance by K-doping. Chem Eng J 421:127760–127767. https://doi.org/10.1016/j.cej.2020.127760

[29] Zhang LL, Wei C, Fu XY et al (2021) Ternary Ni-based Prussian blue analogue with superior sodium storage performance induced by synergistic effect of Co and Fe. Carbon Energy 3:827–839. https://doi.org/10.1002/cey2.142

[30] Chen ZY, Fu XY, Zhang LL et al (2022) High-performance Fe-based Prussian blue cathode material for enhancing the activity of low-spin Fe by Cu doping. ACS Appl Mater Interfaces 14:5506–5513. https://doi.org/10.1021/acsami.1c23793

[31] Zhang LL, Chen ZY, Fu XY et al (2022) Effect of Zn-substitution induced structural regulation on sodium storage performance of Fe-based Prussian blue. Chem Eng J 433:133739–133746. https://doi.org/10.1016/j.cej.2021.133739

[32] Huang B, Liu Y, Lu Z et al (2019) Prussian blue [K_2 FeFe(CN)$_6$] doped with nickel as a superior cathode: an efficient strategy to enhance Potassiu-m storage performance. ACS Sustain Chem Eng 7:16659–16667. https://doi.org/10.1021/acssuschemeng.9b04012

[33] Huang B, Shao Y, Liu Y, Lu Z, Lu X, Liao S (2019) Improving potassium-ion batteries by optimizing the composition of Prussian blue cathode. ACS Appl Energy Mater 2:6528–6535. https://doi.org/10.1021/acsaem.9b01097

[34] Jiang L, Lu Y, Zhao C et al (2019) Building aqueous K-ion batteries for energy storage. Nat Energy 4:495–503. https://doi.org/10.1038/s41560-019-0388-0

[35] Ge J, Fan L, Rao AM et al (2022) Surface-substituted Prussian blue analogue cathode for sustainable potassium-ion batteries. Nat Sustain 53:225–234. https://doi.org/10.1038/s41893-021-00810-7

[36] Bie X, Kubota K, Hosaka T, Chihara K, Komaba S (2017) A novel K-ion battery: hexacyanoferrate(ii)/graphite cell. J Mater Chem 5:4325–4330. https://doi.org/10.1039/C7TA00220

[37] Moritomo Y, Urase S, Shibata T (2016) Enhanced battery performance in manganese hexacyanoferrate by partial substitution. Electrochim Acta 210:963–969. https://doi.org/10.1016/j.electacta.2016.05.205